

# Polarization orientation dependence of the far infrared spectra of oriented single crystals of 1,3,5-trinitro-S-triazine (RDX) using terahertz time-domain spectroscopy

V. H. Whitley · D. E. Hooks · K. J. Ramos ·  
J. F. O'Hara · A. K. Azad · A. J. Taylor · J. Barber ·  
R. D. Averitt

Received: 22 January 2009 / Revised: 24 February 2009 / Accepted: 5 March 2009 / Published online: 28 March 2009  
© Springer-Verlag 2009

**Abstract** The far infrared spectra of (100), (010), and (001)-oriented RDX single crystals were measured as the crystal was rotated about the axis perpendicular to the polarization plane of the incident radiation. Absorption measurements were taken at temperatures of both 20 K and 295 K for all rotations using terahertz time-domain spectroscopy. A number of discrete absorptions were found ranging from 10–100 cm<sup>-1</sup> (0.3–3 THz). The absorptions are highly dependent on the orientation of the terahertz polarization with respect to crystallographic axes.

**Keywords** IR spectroscopy/Raman spectroscopy · Organic compounds/trace organic compounds · Spectroscopy/instrumentation

## Introduction

Terahertz time-domain spectroscopy (THz-TDS) shows potential as a noninvasive technique for the detection of

explosives. Common energetic materials such as RDX, HMX, PETN, and TNT have unique spectral signatures in the <100 cm<sup>-1</sup> range [1–15]. At visible wavelengths, many explosives look remarkably similar to common baking ingredients such as sugar or modeling clay but have unique signatures in the THz range (e.g., below 100 cm<sup>-1</sup>) will pass through visibly opaque materials such as clothing, luggage, paper, etc. Thus, THz radiation can be used to positively identify unknown substances insides opaque materials—a highly useful trait for security applications [3, 16, 17].

While well-characterized [1, 6, 9], the spectrum of RDX below 100 cm<sup>-1</sup> is poorly understood. Measurements on powdered RDX give an absorption spectrum that is an average over many randomly oriented crystals. To complicate matters, the manufacturing process has some effect on the convoluted spectrum as well. Absorption spectra measured on RDX from different manufacturers show significant variation [18]. Assignment of absorptions to the vibrational modes of the crystal structure is difficult when using powders because the high density of absorptions make distinguishing each individual peak difficult and each absorption cannot be assigned to a given crystal orientation. Calculations on isolated RDX molecules are not able to properly account for the interactions measured in the solid phase as the majority of the absorptions seen in the solid phase are intermolecular in character [19]. Progress has been made recently into the calculated spectra of HMX and PETN in the solid phase [20–22], but RDX is a more difficult computational problem due to the large number of molecules in the unit cell ( $Z=8$  for  $\alpha$ -RDX [23],  $Z=2$  for  $\beta$ -HMX [24],  $Z=2$  for PETN [25]). Recent work by Allis et al. [26] has produced reasonable agreement with powdered RDX.

V. H. Whitley (✉) · D. E. Hooks · K. J. Ramos  
DE Division, Los Alamos National Laboratory,  
Los Alamos, NM 87545, USA  
e-mail: vwhitley@lanl.gov

J. F. O'Hara · A. K. Azad · A. J. Taylor  
MPA-CINT, Los Alamos National Laboratory,  
Los Alamos, NM 87545, USA

J. Barber  
Battelle, 2900 Fire Rd., Suite 201,  
Egg Harbor Twp, NJ 08234, USA

R. D. Averitt  
Department of Physics, Boston University,  
Boston, MA 02215, USA

Report Documentation Page			Form Approved OMB No. 0704-0188	
<p>Public reporting burden for the collection of information is estimated to average 1 hour per response, including the time for reviewing instructions, searching existing data sources, gathering and maintaining the data needed, and completing and reviewing the collection of information. Send comments regarding this burden estimate or any other aspect of this collection of information, including suggestions for reducing this burden, to Washington Headquarters Services, Directorate for Information Operations and Reports, 1215 Jefferson Davis Highway, Suite 1204, Arlington VA 22202-4302. Respondents should be aware that notwithstanding any other provision of law, no person shall be subject to a penalty for failing to comply with a collection of information if it does not display a currently valid OMB control number.</p>				
1. REPORT DATE <b>FEB 2009</b>	2. REPORT TYPE	3. DATES COVERED <b>00-00-2009 to 00-00-2009</b>		
4. TITLE AND SUBTITLE <b>Polarization orientation dependence of the far infrared spectra of oriented single crystals of 1,3,5-trinitro-S-triazine (RDX) using terahertz time-domain spectroscopy</b>			5a. CONTRACT NUMBER	
			5b. GRANT NUMBER	
			5c. PROGRAM ELEMENT NUMBER	
6. AUTHOR(S) <b>Boston University ,Department of Physics,Boston,MA,02215</b>			5d. PROJECT NUMBER	
			5e. TASK NUMBER	
			5f. WORK UNIT NUMBER	
7. PERFORMING ORGANIZATION NAME(S) AND ADDRESS(ES) <b>Boston University ,Department of Physics,Boston,MA,02215</b>			8. PERFORMING ORGANIZATION REPORT NUMBER	
			10. SPONSOR/MONITOR'S ACRONYM(S)	
9. SPONSORING/MONITORING AGENCY NAME(S) AND ADDRESS(ES)			11. SPONSOR/MONITOR'S REPORT NUMBER(S)	
			12. DISTRIBUTION/AVAILABILITY STATEMENT <b>Approved for public release; distribution unlimited</b>	
13. SUPPLEMENTARY NOTES				
14. ABSTRACT <p><b>The far infrared spectra of (100), (010), and (001)-oriented RDX single crystals were measured as the crystal was rotated about the axis perpendicular to the polarization plane of the incident radiation. Absorption measurements were taken at temperatures of both 20 K and 295 K for all rotations using terahertz time-domain spectroscopy. A number of discrete absorptions were found ranging from 10-100 cm<sup>-1</sup> (0.3-3 THz). The absorptions are highly dependent on the orientation of the terahertz polarization with respect to crystallographic axes.</b></p>				
15. SUBJECT TERMS				
16. SECURITY CLASSIFICATION OF:			17. LIMITATION OF ABSTRACT <b>Same as Report (SAR)</b>	18. NUMBER OF PAGES <b>8</b>
a. REPORT <b>unclassified</b>	b. ABSTRACT <b>unclassified</b>	c. THIS PAGE <b>unclassified</b>		
19a. NAME OF RESPONSIBLE PERSON				

Developing models that can correctly characterize the complex absorption patterns of RDX in the  $<100\text{ cm}^{-1}$  region is critically important. This phonon-rich region of the spectrum contains information relevant to the validation of equation of state parameters used to model the detonation process. Accurate modeling would help clarify the role these phonon modes play in shock-initiation of explosives. It has been postulated that energy is funneled from the shock into individual molecules through multiphonon up-pumping via delocalized low-frequency ( $<6\text{ THz}$ ) phonons [27–30], but little experimental data on these phonon modes exist.

In an effort to resolve and identify the vibrational modes of RDX, single crystals of  $\alpha$ -RDX have been studied via THz-TDS. This work is a continuation of the study published by Barber et al. in 2005 [19]. Crystals cut at three orthogonal orientations were mounted and oriented via X-ray diffraction. An azimuthal rotation stage with a center hole for performing transmission spectroscopy was mounted to a cryostat, enabling spectra to be collected at  $\sim 20\text{ K}$ . The results of this study show terahertz absorptions not previously observed from powders or formulations.

## Experimental section

For these measurements, five different RDX samples were used—two (100)-oriented samples, two (010)-oriented samples, and one (001)-oriented sample. The samples were cut from large single crystals, nominally 5 cm on a side. UK-manufactured RDX was dried, purified by Soxhlet extraction in acetone and recrystallized in acetone prior to use. The crystals were grown by slow evaporation of acetone at  $32\text{ }^\circ\text{C}$ , in a 1,000 mL, spoutless beaker covered by a Parafilm-coated watch glass. The bottom third of the beaker was immersed in a heating bath and the top was open to air at room temperature. This method allowed for convective mixing and the reflux continuously washed the beaker sides preventing parasitic growth. Seeds were grown from acetone by a similar procedure.

Contact goniometry was used to locate planes in RDX by redundant reference to crystal facets. The samples were cut using a low-speed diamond impregnated wire saw using a solution of Alconox in deionized water as a lubricant. Samples were measured in an as-cut configuration; no further polishing was performed. RDX crystals are extremely fragile, limiting the minimum sample thickness that can be cut without fracture to approximately 1 mm. The (001)- and (010)-oriented samples were nominally 1 mm thick, the (100) sample was 1.5 mm thick. All samples were approximately 1 cm  $\times$  1 cm wide. The orientations of the crystallographic axis and the orientation of the in-plane axes were verified by transmission Laue X-ray diffraction. Typically, the uncertainty in axis orientation is within one-

half degree of the reported face. Plane indices are given with respect to the *Pbca* space group of RDX [23]. The structure of the RDX crystal cut along the (100), (010), and (001) faces is shown in Fig. 1.

The THz-TDS system was similar to those used in previous work [31] with some modifications to accommodate the specialized helium cryostat. Photoconductive antennas backed with silicon lenses served to both generate and detect the collimated THz radiation, while confocal optics guided the THz beam through the samples. The beam was achromatically focused to a spot about 6 mm in diameter at the sample face. The maximum spectral resolution of the system was  $1.1\text{ cm}^{-1}$ . The polarization purity was nominally 100:1, which is typical for photoconductive switch systems.

The cryostat and sample mounting structures were specially made to allow sample rotation and cooling under vacuum. Samples were mounted on the front end of the rotating stage, essentially a copper tube through which the focused THz beam propagated. The tube diameter was sufficiently large to avoid interactions with the THz beam. A ring gear was attached to the back of the tube and engaged to a pinion gear that was magnetically coupled through the vacuum chamber to a computer-controlled stepper motor. This allowed accurate rotational stepping of the sample orientation under vacuum. The tube was thermally connected to the main cryostat cold finger by a flexible copper band. The thermal link was sufficient to reduce the sample temperature to  $18\text{ K}$  without interfering with sample rotation. Sample temperatures were monitored by a silicon sensor attached adjacent to the sample.

Initial mounting of the samples into the cryostat and orientation of the rotation stage introduced an angular inaccuracy within approximately  $+/-3^\circ$ . Samples were cooled in a helium cryostat at  $0.025\text{ K/s}$  to avoid cracking. Even at these rates, one each of the (010) and (100) samples cracked. Comparisons of the absorptions of the cracked and uncracked samples show that the cracks produced no significant variations in the data. Over the full  $180^\circ$  rotation, the sample temperature ranged from  $18\text{--}23\text{ K}$  and had a maximum variation of  $0.5\text{ K}$  during any one scan. The variation in temperature was caused by the varying thermal link of the rotation stage as it changed position. Based on the temperature-dependent absorption measurements of RDX by Melinger [15], Barber [19], and Burnett [32], the shape and position of the spectra are expected to remain unchanged over this temperature variation.

## Analysis

The time-domain data were acquired for each sample orientation over a  $180^\circ$  rotation around the primary crystallographic axis using angle increments of  $9^\circ$  at  $22\text{ K}$  and  $22.5^\circ$  at  $295\text{ K}$ . Reference data sets with the sample

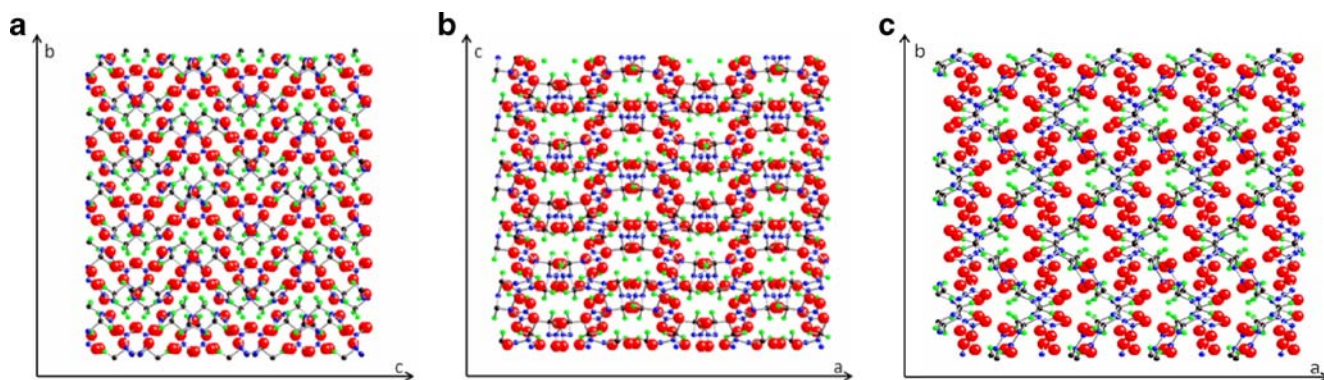


**Fig. 1** Representation of RDX along the primary directions **a** 100 **b** 010 **c** 001. Carbon is shown in black, nitrogen in blue, hydrogen in green, and oxygen in red

moved out of the path of the beam were taken at the beginning and end of each sample data set. The ratio of the Fourier-transformed THz-TDS sample data to a reference data set yielded the complex transmission function. Figure 2 shows the results of a typical terahertz reference amplitude. Also shown are the transmission amplitude through RDX (010) with the polarization oriented along the *c*-axis and the noise level of the detector/lock-in amplifier. The system is capable of producing measurable quantities of radiation to  $150\text{ cm}^{-1}$ . The combination of decreased emission amplitude above  $\sim 100\text{ cm}^{-1}$  and strong sample absorption resulted in noisy, inconsistent data. None of the data above  $100\text{ cm}^{-1}$  is discussed in this paper, but the data to  $135\text{ cm}^{-1}$  is included in the data files in the electronic supplemental material. Strong absorption features, such as the  $57\text{ cm}^{-1}$  feature shown in Fig. 2, are completely absorbing. Since the minimum transmission is not measurable, the data produces an artificial maximum value of the absorption index  $\kappa$  or the power absorption coefficient  $\alpha$ .

Since the samples are homogenous single-crystal specimen with planar faces and known thicknesses, indices of refraction and absorption values as a function of crystal orientation can be extracted. Initially, a Beer's law analysis was used to determine measured absorption coefficients (not correcting for Fresnel reflections) through the sample at each orientation. This was refined by extracting the complex index of refraction  $n$  and absorption index  $\kappa$  from the THz-TDS data using the method of Duvillaret et al. [33]. The similarity of the two methods provided a check that the fitting routines were working correctly. The fits were also verified by running the extracted results through the forward propagation equation, which matched the measured data.

## Results and discussions

Figures 3–4 show the angular dependence of  $\kappa$ - and  $n$ -values for samples of RDX (100), (010), and (001) taken at

20 K. The data are presented as radial contour plots with the THz absorption spectrum extending radially outward from the center to a maximum of  $100\text{ cm}^{-1}$ . Dashed circles indicate  $20\text{ cm}^{-1}$  increments. The values of  $n$ - or  $\kappa$ - are plotted as a function of rotation about the sample. Principle in-plane axes are indicated on the plots. Since data were taken over  $180^\circ$  of rotation instead of a full  $360^\circ$  rotation, the data were reproduced over the  $180$ – $360^\circ$  range to generate a full rotation spectrum. RDX has C2 symmetry so data from  $0$ – $180^\circ$  should be identical to  $180$ – $360^\circ$ . The reader should take some caution with regions of the spectrum showing strong absorption. These absorptions are strong enough to completely block all incident THz radiation, so that the absorption values in these locations should be considered as a minimum instead of exact.

All three orientations of RDX in Fig. 3 show a complex, feature-rich absorption structure. Significant absorption features extend from as low as  $12\text{ cm}^{-1}$  to well above  $100\text{ cm}^{-1}$ . Below  $\sim 80\text{ cm}^{-1}$ , RDX has a number of

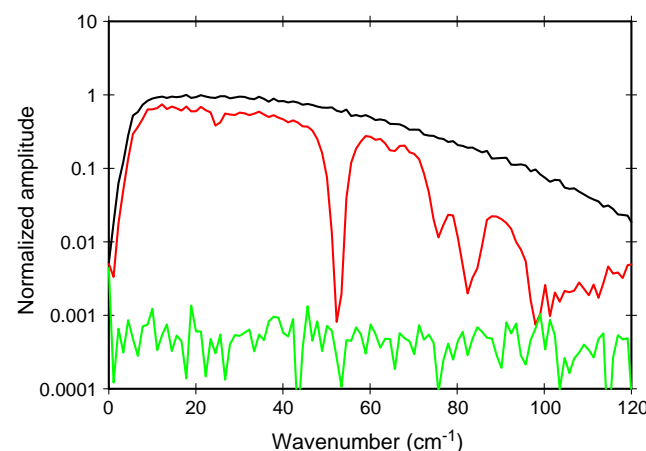


**Fig. 2** Electric field amplitude of the THz spectral emission with no sample (black), through (010) RDX with the polarization oriented along the *c*-axis (red), and the noise level of the detector/lock-in amplifier (green)

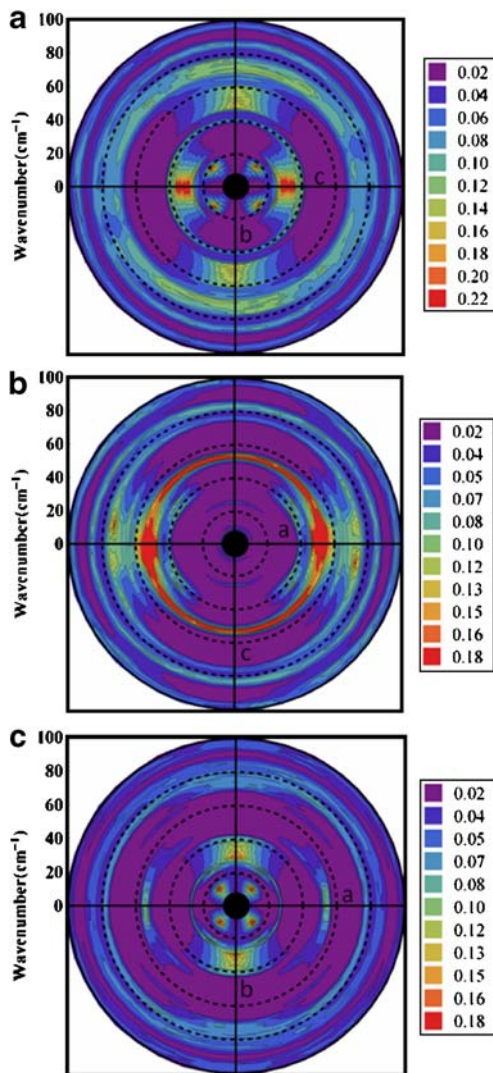


**Fig. 3** Comparison of the absorption index  $\kappa$  of RDX(100), RDX(010), and RDX(001) over the 7–100  $\text{cm}^{-1}$  range at  $T=20$  K. The dashed circles correspond to 20  $\text{cm}^{-1}$  wavenumber intervals. Crystallographic axes are shown as the labeled solid lines

rotationally dependent absorptions strongly correlated to its crystallographic orientation with respect to the THz polarization, above  $\sim 80 \text{ cm}^{-1}$ , absorptions are generally rotationally invariant.

Broad absorption features below 80  $\text{cm}^{-1}$  are found along the primary crystallographic axes. The  $b$ -axis has a broad absorption from 27–42  $\text{cm}^{-1}$  in (001)-oriented RDX and from 48–60  $\text{cm}^{-1}$  in (100)-oriented RDX. The  $a$ -axis has a broad absorption from 55  $\text{cm}^{-1}$  to 59  $\text{cm}^{-1}$  seen in both the RDX(010) and RDX(001) orientations. The  $c$ -axis has a broad absorption from 25–40  $\text{cm}^{-1}$  in the (100) orientation, although there is no corresponding  $c$ -axis absorption in the (010)-oriented material. In addition, there are two broad low-frequency absorptions located at 45° between in-plane axes. RDX(100) shows an absorption at 18  $\text{cm}^{-1}$  located between the  $b$ - and  $c$ -axes and RDX(010)

shows an absorption at 12  $\text{cm}^{-1}$  located between the  $a$ - and  $b$ -axes.

Narrow, rotationally invariant absorptions with 1  $\text{cm}^{-1}$  FWHM are found at 40  $\text{cm}^{-1}$  in RDX(100), 55  $\text{cm}^{-1}$  in RDX(010), and at 25  $\text{cm}^{-1}$  in RDX(001). Narrow, orientation-dependent absorptions associated with the  $c$ -axis are seen in the (100) and (010) orientations at 27  $\text{cm}^{-1}$ . Other narrow absorptions are roughly located equally between the primary in-plane axes at 24  $\text{cm}^{-1}$ , 48  $\text{cm}^{-1}$ , 67  $\text{cm}^{-1}$  in RDX (001) and 40  $\text{cm}^{-1}$  and 45  $\text{cm}^{-1}$  in RDX (010). A summary of the in-plane absorptions found in RDX is listed in Table 1.

The absorbing states below 40  $\text{cm}^{-1}$  in RDX are unique when compared to HMX [34] or PETN [34]. HMX and PETN do not show absorptions at such low frequencies. The lowest absorption for PETN is 55  $\text{cm}^{-1}$  and for HMX

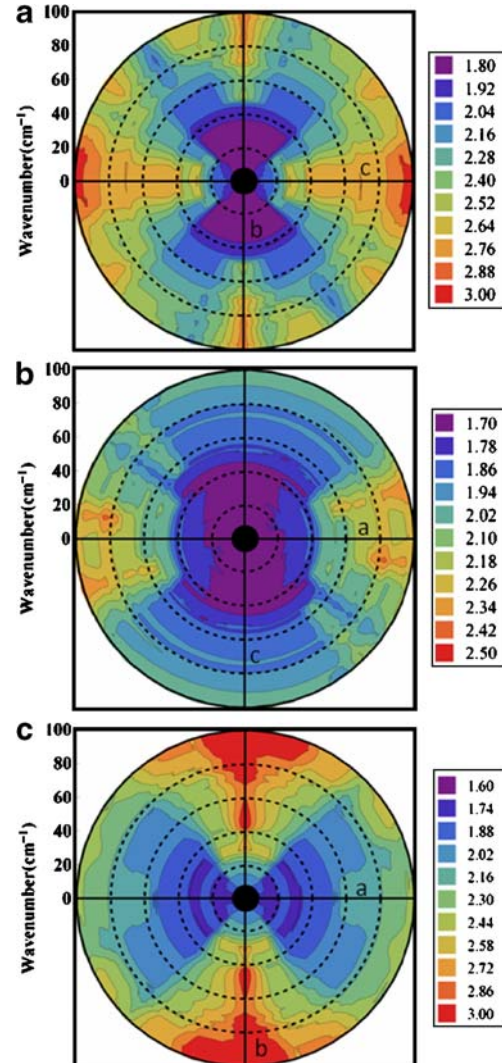


**Fig. 4** Comparison of the index of refraction of RDX(100), RDX(010), and RDX(001) from 7–100  $\text{cm}^{-1}$  at  $T=20$  K. Crystallographic axes are shown as the labeled solid lines

**Table 1** Summary of absorption found in (100)-, (010)-, and (001)-oriented RDX

Orientation	Frequency cm <sup>-1</sup> 22K	Frequency cm <sup>-1</sup> 295K	Absorption Index (κ)	Absorption coefficient α (cm <sup>-1</sup> )	Relation to axes
(100)	17.6	14.2	0.19	42	45° between <i>b,c</i>
	25.4		0.14	45	<i>c</i> -axis
	27-37	22-37	0.23	78	<i>c</i> -axis
	39.5		0.07	35	R.I
	46-61	40-58	0.15	87-115	<i>b</i> -axis
	66.7-77.3	>60	0.12	>75	R.I
	83.3-87.5		0.09	>94	R.I
	94-97		0.09	>106	R.I
(010)	25	19.8	0.05	16	<i>c</i> -axis
	38.3	38.8	0.10	48	30° from <i>a</i> -axis
	42.2		0.10	53	30° from <i>a</i> -axis
	46-60	42-53	0.18	104-135	<i>c</i> -axis
	51.54	48.4	0.15	91-101	R.I
	64.3		0.10	81	<i>a</i> -axis
	67-77	66-72	0.13	>110	<i>a</i> -axis
	75.5		0.06	>56	R.I
(001)	82-86		0.08	>82	R.I
	>94		0.08	>94	R.I
	13.8	10.3	0.18	31	45° between <i>a,b</i>
	23.2		0.08	23	30° from <i>b</i> -axis
	26.5	18.9	0.05	17	R.I. and 30° from <i>b</i> -axis
	28.41	20-38	0.14	50-72	<i>b</i> -axis
	48.3	43.5	0.04	24	45° between <i>a, b</i>
	51-56	46-51	0.09	58-63	<i>a</i> -axis
	65.3	58-67	0.03	>46	45° between <i>a, b</i>
	68.9		0.05	>43	15° from <i>b</i> -axis
	69-75		0.07	>61	<i>b</i> -axis
	75-79	>68	0.07	>66	R.I.
	82-89		0.07	>72	R.I.
	93.2		0.04	>47	30° from <i>b</i> -axis
	94-99		0.04	>47	<i>b</i> -axis
	>97		0.04	>49	R.I.

Rotationally invariant absorptions are listed as ‘R.I.’ in the table

is 40 cm<sup>-1</sup>. The causes of the low-frequency absorption in RDX are thought to be related to the six extra molecules in the unit cell compared to PETN and HMX and the larger unit cell of RDX (13.192–11.574–10.709 Å for RDX [23] compared to 9.380–9.380–6.71 Å for PETN(I) [25] and 6.54–11.05–8.7 Å for HMX [24]). The absorption peaks of RDX in the 25–30 cm<sup>-1</sup> range are particularly significant because they are responsible for the ~27 cm<sup>-1</sup> “fingerprint” peak of powdered RDX. The absorptions of single-crystal RDX below 27 cm<sup>-1</sup>, namely the broad peaks located at 18 cm<sup>-1</sup> and 12 cm<sup>-1</sup> in RDX(100) and (001), respectively, have not been previously reported. In the powdered

spectrum, the 27 cm<sup>-1</sup> absorption is a broad dominant feature that masks the 12 cm<sup>-1</sup> and 18 cm<sup>-1</sup> absorptions.

Figure 4 shows the frequency-dependent index of refraction of single-crystal RDX as a function of orientation. The index of refraction increases from ~1.6 to ~3 over the frequency range of 7–100 cm<sup>-1</sup>. RDX, known to be birefringent in the visible region [35], is also birefringent in the 7–100 cm<sup>-1</sup> range. Symmetry points in the angular variation of the index of refraction correspond identically with the primary in-plane axes.

This birefringence can be used to find the principle in-plane axes of RDX using THz-TDS. The time delay

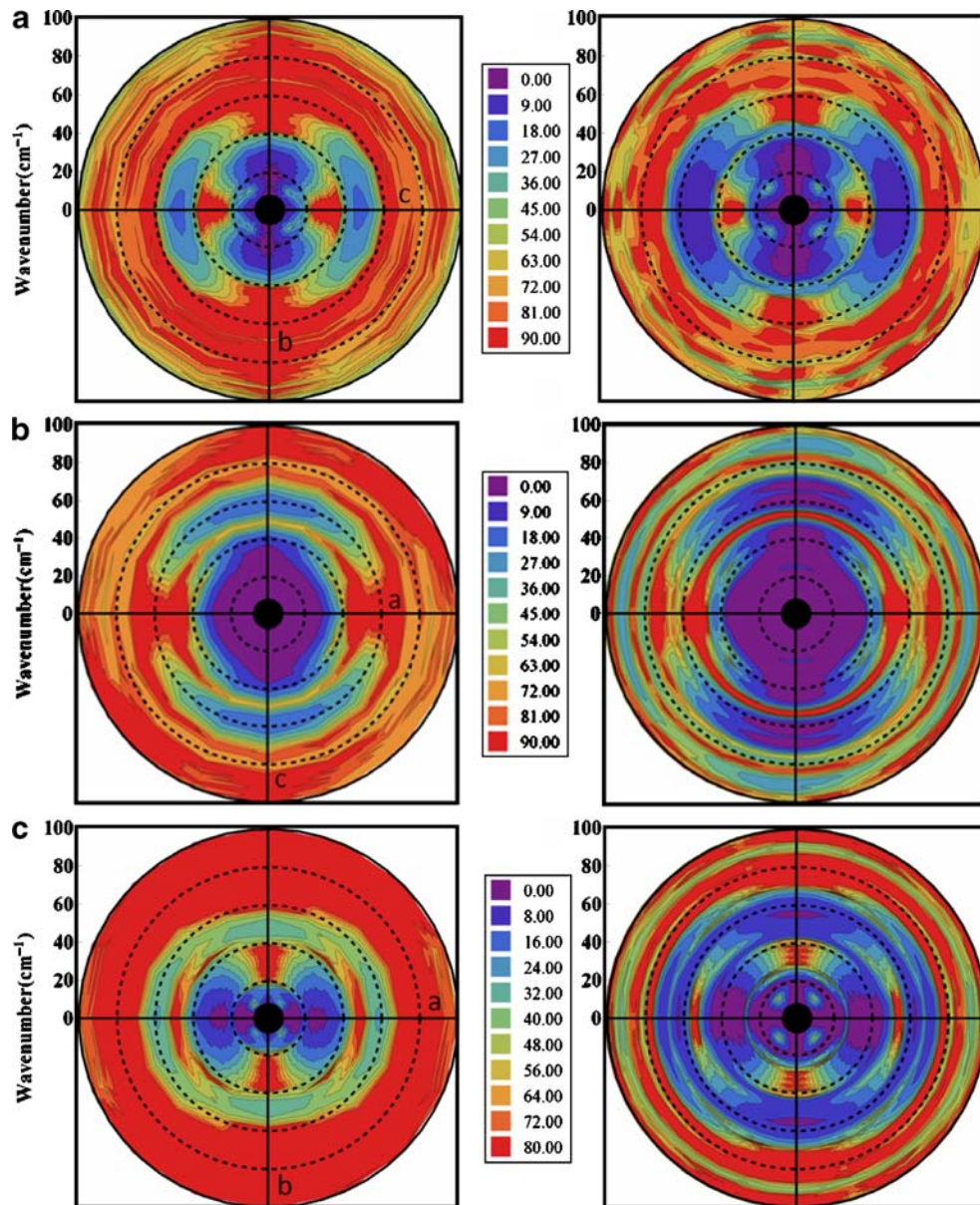
in the onset of the THz-TDS data varies as a function of orientation. The extremes of the measured time delay give the two in-plane axes. The minimum time delay corresponds to the axes with the smaller indices of refraction and the maximum time delay corresponds to the larger indices of refraction. For example, the minimum time delay in the pulse envelope of RDX(100) would locate the *b*-axis and the maximum delay would determine the *c*-axis.

Figure 5 shows a comparison of the power absorption coefficients of the three orthogonal orientations taken at 295 K and 20 K. The absorption coefficients were determined through Beer's law analysis of the data and have not been corrected for Fresnel reflections. The

absorption spectra of RDX at 295 K are very similar to the absorption spectra at 22 K for all orientations. Upon cooling the samples, the spectral features become sharper and shift to higher frequencies. No other major changes in the absorption are found. A summary of the frequency shifts due to temperature are included in Table 1.

This is the first work to present the rotational dependence of the absorptions of RDX single crystals, so comparison with other published work is not possible. We measured two different RDX(010) and RDX(100) samples, and performed two different measurements on the same RDX(001) sample to ensure that the data were reproducible. There were no major sample-to-sample or measurement-to-measurement differences in the absorption spectra. This

**Fig. 5** Comparison of the power absorption coefficient  $\alpha$  for RDX(100) at 295 K (left) and at 20 K (right) for **a** RDX(100), **b** RDX(010), and **c** RDX(001) over the 7–100  $\text{cm}^{-1}$  spectral range. The dashed circles correspond to 20  $\text{cm}^{-1}$  wavenumber intervals. The contour intervals give the absorption coefficient in units of  $\text{cm}^{-1}$



study does overlap with the work of Barber et al. presenting the absorption spectrum of RDX(100) along a single random orientation from 20–295 K [19]. Comparing that spectrum with the RDX(100) absorptions shown above indicates that the sample used by Barber et al. was roughly oriented along the *b*-axis in relation to the THz polarization.

An averaged absorption spectrum of all the angular contributions can be compared to powder spectra if we assume that the powder spectrum is composed of an equally weighted contribution from all possible crystal orientations. To generate the equivalent of a powder absorption coefficient, we first calculate the average measured light intensity as a function of the various angles measured from all three crystal orientations:

$$\left\langle \frac{I}{I_0} \right\rangle = \frac{\sum_{\theta}^n \text{Exp}(-\alpha_{\theta}t)}{n} \quad (1)$$

where  $\alpha_{\theta}$  is the absorption coefficient from a given angular contribution,  $t$  is the thickness of the sample, and  $n$  is the number of angular contributions measured. We are able to calculate this averaged intensity using the values of  $\kappa$  from Fig. 3, and relating the absorption coefficient  $\alpha$  to the absorption index  $\kappa$  and wavelength  $\lambda$  by:  $\alpha=4\pi\kappa/\lambda$ . Once we have the average measured light intensity from an equal distribution of angles, then we can calculate an average absorption coefficient by solving Beer's law:

$$\langle \alpha \rangle = -\ln \left[ \left\langle \frac{I}{I_0} \right\rangle \right] / t \quad (2)$$

Figure 6 shows the results of this analysis using the values of  $\kappa$  determined from all three orientations of RDX at 22 K. Care should be taken when viewing the averaged

spectrum because the values of absorption index  $\kappa$  determined for the strongest absorptions in Fig. 3 are artificially truncated due to dynamic range limitations, so their contributions to the average spectrum will be artificially lowered. Nevertheless, strong absorptions are found at 27, 40, 51–53, 75, 83, and 96 cm<sup>-1</sup>. Allis et al. [26] and Burnett et al. [32] measured the spectrum of powdered RDX at 5 K. There are similarities between our calculated powdered spectrum and the measured spectrum; however, they are not identical. Perhaps the measured powder spectrum is not a true representation of all crystal orientation. Crystal morphology may cause the crystals to pack along given orientations. We also do not know how the surface effects contribute to the total RDX powder spectrum. Surface-related spectral features will be much more prominent when using powders compared to single crystals.

Melinger et al. [15] measured high resolution absorption of ordered polycrystalline RDX films at 13 K, finding 19 separate peaks between 0–116 cm<sup>-1</sup>. It is unclear how those peaks compare to this work or to the powdered spectrum of Burnett. If the films consisted of preferentially oriented polycrystalline RDX, as the authors suggest, we could not decipher a single orientation of the RDX films necessary to compare with the data in this paper. Perhaps the thin film sample was composed of several orientations with respect to the surface and the THz polarization.

## Conclusions

We present absorption spectra of RDX (100), (010) and (001) from 7–100 cm<sup>-1</sup> at 295 K and 20 K as a function of orientation with respect to THz polarization. Results demonstrate the expected dependence of spectral features on angular orientation through alignment of the oscillating dipole to the THz field. Absorptions as low as 12 cm<sup>-1</sup> have been observed, the lowest frequency absorptions reported for RDX to date. Line widths are predominantly broad (10 cm<sup>-1</sup> FWHM), with some modes as narrow as 1 cm<sup>-1</sup>. It should be possible to make assignments for the spectrally resolved absorptions by comparing these results with normal mode calculations of an  $\alpha$ -RDX crystal.

**Acknowledgments** The authors wish to thank Frank Abeyta for sample holder design and fabrication. This work was supported in part by the Office of Naval Research and was performed at Los Alamos National Laboratory, operated by Los Alamos National Security, LLC, for the National Nuclear Security Administration of the U.S. Department of Energy under contract DE-AC52-06NA25396. Jeffrey Barber was supported in part by the Department of Homeland Security under contract DTFACIT-03-C-00042.

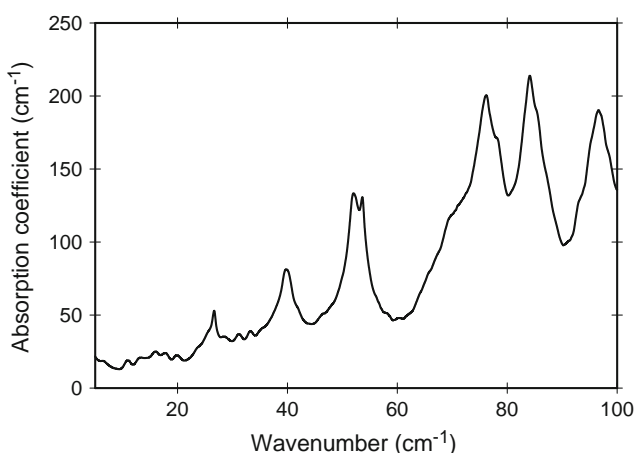


**Fig. 6** Average spectrum of single crystal RDX at 20 K composed of an equally weighted average of all the angular contributions

## References

1. Kemp MC, Taday PF, Cole BE, Cluff JA, Fitzgerald AJ, Tribe WR (2003) Proc SPIE 5070:44
2. Huang F, Schulkin B, Altan H, Federici JF, Gary D, Barat R, Zimdars D, Chen M, Tanner DB (2004) Appl Phys Lett 85:5535
3. Yamamoto K, Yamaguchi M, Miyamaru F, Tani M, Hangyo M, Ikeda T, Matsushita A, Koide K, Tatsuno M, Minami Y (2004) Jpn J Appl Phys Part 2 43:L414
4. Chen Y, Liu H, Deng Y, Veksler D, Shur M et al (2004) Proc SPIE 5411:1
5. Shen YC, Lo T, Taday PF, Cole BE, Tribe WR, Kemp MC (2005) Appl Phys Lett 86:241116
6. Cook DJ, Decker BK, Allen MG (2005) Quantitative THz Spectroscopy of Explosive Materials. In: *Optical Terahertz Science and Technology*, Technical Digest (CD) (Optical Society of America, 2005), paper MA6. <http://www.opticsinfobase.org/abstract.cfm?URI=OTST-2005-MA6>
7. Hu Y, Huang P, Guo L, Wang X, Zhang C (2006) Phys Lett A359:728
8. Zhong H, Redo-Sanchez A, Zhang XC (2006) Opt Express 14:9130
9. Leahy-Hoppa MR, Fitch MJ, Zheng X, Hayden LM, Osiander R (2007) Chem Phys Lett 434:227
10. Fan WH, Burnett A, Upadhyia PC, Cunningham J, Linfield EH, Davies AG (2007) Appl Spectrosc 61:638
11. Fitch MJ, Leahy-Hoppa MR, Ott EW, Osiander R (2007) Chem Phys Lett 443:284
12. Chen J, Chen Y, Zhao H, Bastiaans GJ, Zhang XC (2007) Opt Express 15:12060
13. Baker C, Lo T, Tribe WR, Cole BE, Hogbin MR, Kemp MC (2007) Proc IEEE 95:1559
14. Laman N, Sree Harsha S, Grischkowsky D, Melinger JS (2008) Opt Express 16:4094
15. Melinger JS, Laman N, Grischkowsky D (2008) Appl Phys Lett 93:011102
16. Tribe WR, Newnham DA, Taday PF, Kemp MC (2004) Proc SPIE 5354:168
17. Watters DG, Falconer DG, Harker KJ, Ueberschaer R, Bahr AJ (1995) Res Nondestructive Evaluation 7:153
18. Wilkinson J, Caulder SM, Portieri A (2008) Proc SPIE 6949:694904
19. Barber J, Hooks DE, Funk DJ, Averitt RD, Taylor AJ, Babikov D (2005) J Phys Chem A109:3501
20. Allis DG, Korter TM (2006) ChemPhysChem 7:2398
21. Allis DG, Prokhorova DA, Korter TM (2006) J Phys Chem A110:1951
22. Velizhanin KA, Kilina S, Sewell TD, Piryatinski A (2008) J Phys Chem B112:13252
23. Choi CS, Prince E (1972) Acta Crystallogr B28:2857
24. Cady HH, Larson AC, Cromer DT (1963) Acta Crystallogr 16:617
25. Cady HH, Larson AC (1975) Acta Crystallogr B31:1864
26. Allis DG, Zeitler JA, Taday PF, Korter TM (2008) Chem Phys Lett 463:84
27. Fried LE, Ruggiero AJ (1994) J Phys Chem 98:9786
28. Tokmakoff A, Fayer MD, Dlott DD (1993) J Phys Chem 97:1901
29. Walker FE (1988) J Appl Phys 63:5548
30. Zerilli FJ, Toton ET (1984) Phys Rev B29:5891
31. O'Hara JF, Zide JMO, Gossard AC, Taylor AJ, Averitt RD (2006) Appl Phys Lett 88:251119
32. Burnett AD, Fan WH, Upadhyia PC, Cunningham JE, Edwards HGM, Kendrick J, Munshi T, Hargreaves M, Linfield EH, Davies AG (2007) Proc SPIE 6549:654905
33. Duvillaret L, Garet F, Coutaz JL (1996) IEEE J Sel Top Quantum Electron 2:739
34. Whitley VH, Hooks DE, Ramos KJ, O'Hara JF, Azad AK, Barber J, Averitt RD (2009) *In Preparation*
35. Gibbs TR, Popolato A (1980) LASL explosive property data. University of California Press, Berkley, CA